Journal of Materials Chemistry A

ROYAL SOCIETY OF CHEMISTRY

PAPER

View Article Online
View Journal | View Issue

Cite this: J. Mater. Chem. A, 2022, 10, 20035

Effects of the rigid and sterically bulky structure of non-fused nonfullerene acceptors on transient photon-to-current dynamics†

Seihou Jinnai, *[a] Kasumi Murayama,[b] Keisuke Nagai,[a] Megumi Mineshita,[c] Kosaku Kato,[d] Azusa Muraoka,[c] Akira Yamakata, *[d] Akinori Saeki,[ef] Yasuhiro Kobori *[bg] and Yutaka Ie *[af]

Non-fused electron-accepting π-conjugated compounds have been investigated recently for application to nonfullerene acceptors (NFAs) in organic solar cells (OSCs). However, the establishment of rational molecular design for non-fused NFAs is still lagging because the influence of flexible non-fused structures on the dynamics of electron–hole pairs in OSCs is not entirely understood. In this study, we utilized cyclopentene-annelated thiophene with spiro-substituted 2,7-bis(2-ethylhexyl)fluorene (FT) as a rigid and sterically bulky linker unit and developed a non-fused NFA (TT–FT–DCI) containing FT units. Photophysical measurements indicated that the introduction of the FT unit leads to the formation of rigid molecular structure. OSCs based on donor polymer (PBDB-T) and TT–FT–DCI showed an improved power conversion efficiency of 7.13% due to the increase in the short-circuit current density and fill factor. Time-resolved optical and microwave spectroscopies showed that the FT unit contributes to the long lifetimes of excited state and charge-separated state in the PBDBT:TT–FT–DCI blend films. Time-resolved electron paramagnetic resonance measurements showed that the distant charge-separated states of the face-to-face PBDB-T:TT–FT–DCI structure, which is derived by avoiding over-crystallization by the steric bulkiness of TT–FT–DCI, can interact with the cathodes for preferential electron injection following charge generations. This study highlights that by using the rigid π-conjugated framework and suppressed self-aggregation of the non-fused acceptor, effective molecular design for the appropriate dynamics of photocurrent generation is possible.

Received 1st April 2022
Accepted 21st June 2022

DOI: 10.1039/d2ta02604j

rsc.li/materials-a

[a]The Institute of Scientific and Industrial Research (SANKEN), Osaka University, 8-1 Mihogaoka, Osaka 567-0047, Ibaraki, Japan. E-mail: jinnai@sanken.osaka-u.ac.jp; yutakaie@sanken.osaka-u.ac.jp

[b]Department of Chemistry, Graduate School of Science, Kobe University, 1-1 Rokkodai-cho, Nada-ku, Kobe 657-8501, Japan

[c]Department of Mathematics, Physics and Computer Science, Japan Women's University, 2-8-1, Mejirodai, Bunkyo-ku, Tokyo 112-8681, Japan

[d]Graduate School of Natural Science & Technology, Okayama University, 3-1-1 Tsushima-naka, Okayama 700-8530, Japan. E-mail: yamakata@okayama-u.ac.jp

[e]Department of Applied Chemistry, Graduate School of Engineering, Osaka University, 2-1 Yamadaoka, Suita, Osaka 565-0871, Japan

[f]Innovative Catalysis Science Division, Institute for Open and Transdisciplinary Research Initiatives (OTRI), Osaka University, 2-1 Yamadaoka, Suita, Osaka 565-0871, Japan

[g]Molecular Photoscience Research Center, Kobe University, 1-1 Rokkodai-cho, Nada-ku, Kobe 657-8501, Japan. E-mail: ykobori@kitty.kobe-u.ac.jp

† Electronic supplementary information (ESI) available: Detailed synthetic procedures and characterization data for new compounds and additional experimental results. See https://doi.org/10.1039/d2ta02604j

Seihou Jinnai is an Assistant Professor of Department of Soft Nanomaterials (Ie group) in the Institute of Scientific and Industrial Research (SANKEN), Osaka University, Japan. He received his PhD degree from Osaka University in 2017 under the supervision of Professor Yoshio Aso. After he engaged in research on functional organic dyes as a corporate researcher at Orient Chemical Industries Co., Ltd. from 2016 to 2019, he joined the laboratory of Professor Yutaka Ie. His research focus is development of new π-conjugated compounds and systems for organic electronics and photo-functional applications.

1 Introduction

Organic solar cells (OSCs) have been widely investigated as next-generation energy production sources owing to their potential for large-area fabrication, light weight, flexibility, and their ease of use in solution processes.[1–5] The photoactive layer of OSCs is commonly composed of a blend of hole-transporting semiconductors (donors) and electron-transporting semiconductors (acceptors), which form so-called bulk heterojunction structures in the films.[6–8] To make use of π-conjugated systems based on their light absorbance, carrier transport, and ease of frontier energy level, the donor–acceptor (D–A)-type configuration has become a rational molecular design for both the donor and acceptor.[9–16] The development of A–D–A-type nonfullerene acceptors (NFAs) with large fused-ring donor structures, such as Y6 and ITIC, have significantly accelerated OSC research (chemical structures shown in Fig. S1 in the ESI†),[17–20] and the power conversion efficiencies (PCEs) of the state-of-the-art devices have surpassed 19%.[21] Comprehensive studies, including those on steady state current–voltage,[17,18,22–24] spectroscopic,[25–27] and morphological analyses[28–33] have revealed that the utilization of a rigid π-conjugated framework and the suppression of face-to-face intermolecular arrangement are advantageous for photoinduced charge generation and isotropic charge transport. However, the utilization of such fused-ring structures has faced difficulties in scale-up synthesis and structural tunability.[34,35] For instance, Y6 and ITIC synthesized through 10 and 8 synthetic steps, respectively, have limited industrial viability because of the high synthetic complexities.[36,37]

As another emerging molecular design for NFAs, electron-accepting non-fused π-conjugated systems have been extensively developed recently.[38] For recent non-fused NFAs, the rigidity of the π-conjugated framework is reinforced by the introduction of intramolecular S–F[39–43] and S–O[44–48] interactions (types A–C in Fig. 1a). Very recently, it was reported that the head-to-head structures of type D are also effective in improving the rigidity of π-conjugation in non-fused NFA.[49,50] By introducing these intramolecular interactions to the π-conjugated systems, non-fused NFAs have been developed with PCEs over 10%.[44,46,49,50] However, OSCs based on non-fused NFAs are still being developed because of the moderate short-circuit current density (J_{SC}) and fill factor (FF) of OSC characteristics.[40,51] To overcome this problem, the development of new non-fused NFAs is important to establish the guidelines for molecular design. Along this line, it is also essential to clarify the effect of the flexibility of non-fused NFA on the dynamic carrier generation and extraction processes in OSCs.

We have revealed that the incorporation of cyclopentene-annelation into thiophene unit can effectively improve the planarity and rigidity of π-conjugation in its-repeated oligothiophenes (Fig. 1b).[52] In this molecular design, the combination of cyclopentene-annelated thiophene with spiro-substituted 2,7-bis(2-ethylhexyl)fluorene (FT) achieved not only high effective conjugation but also complete encapsulation of π-conjugated backbones because intermolecular π–π interactions between neighboring oligothiophenes are completely suppressed by the 2,7-bis(2-ethylhexyl)fluorene group that is positioned perpendicular to the main chain.[53] Therefore, long oligothiophenes composed of FT units can function as highly conductive molecular wires in single-molecule electronics.[54–56] In this situation, we anticipated that the FT unit would play a significant role in the rigid and sterically bulky effects in non-fused NFAs. In this study, to elucidate the structure–property-OSC functional relationships of NFAs, we designed and synthesized an electron-accepting compound TT–FT–DCI and its reference compound TT–T–DCI, which are composed of thienothiophene (TT) and 3-(dicyanomethylidene)indanone (DCI)[57–59] (Fig. 1c). Detailed comparisons of the physical properties, OSC characteristics, and dynamics of excitons in the donor/acceptor blend films were performed using time-resolved spectroscopy techniques of time-resolved UV-vis and IR absorption spectroscopies, flash-photolysis time-resolved microwave-conductivity (FP-TRMC), and time-resolved electron paramagnetic resonance (TREPR) measurements to evaluate the impact of the presence of the FT unit on photocharge generation in OSCs.

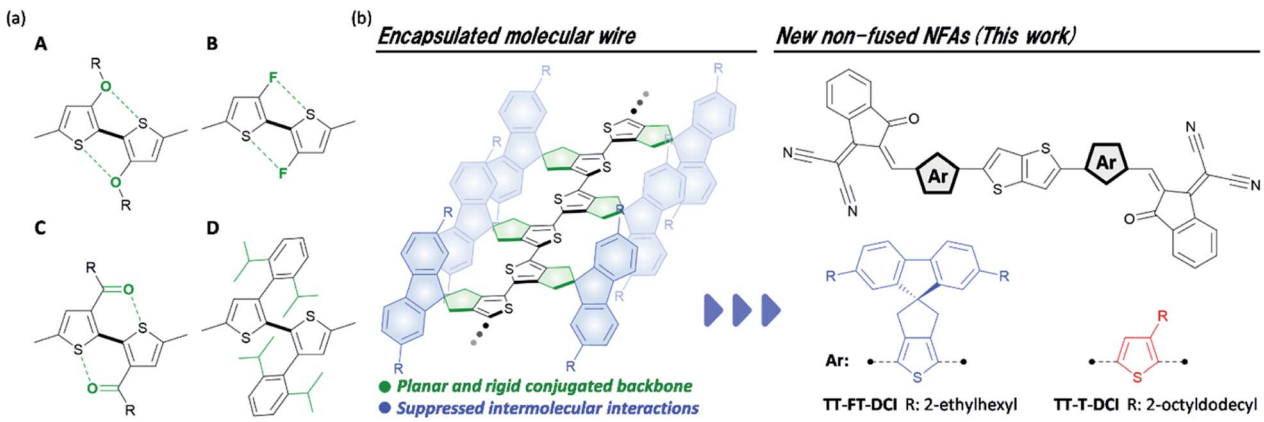

Fig. 1 (a) Typical intramolecular interactions found in non-fused NFAs, (b) chemical structure of encapsulated oligothiophene molecular wire, and non-fused NFAs developed in this study.

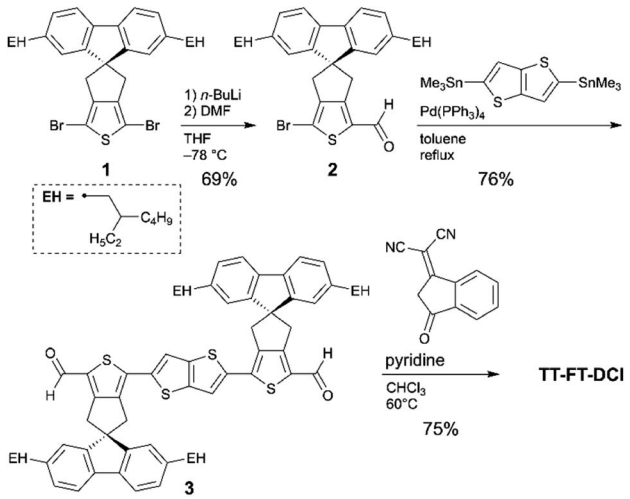

Scheme 1 Synthetic route for TT–FT–DCI.

2 Results and discussion

2.1. Synthesis and thermal properties

The synthetic routes to TT–FT–DCI, TT–T–DCI, TT–T(bo)–DCI, and TT–T(eh)–DCI are shown in Scheme 1. As the starting material for TT–FT–DCI, dibromo FT compound (**1**) was prepared by our reported method.[55] Compound **1** was monolithiated and reacted with *N*,*N*-dimethylformamide (DMF) to synthesize formylated compound **2**. The Migita–Kosugi–Stille coupling between **2** and 2,5-bistrimethylstannylthieno[3,2-*b*] thiophene afforded **3**. Finally, Knoevenagel condensation of **2** with DCI afforded TT–FT–DCI. The other acceptors of TT–T–DCI, TT–T(bo)–DCI, and TT–T(eh)–DCI were synthesized in the same manner (Scheme S1†). As summarized in Table S1,† while TT–T(bo)–DCI and TT–T(eh)–DCI showed limited solubilities of less than 2 mg mL^{-1} in representative process solvents such as chloroform ($CHCl_3$), chlorobenzene, and *o*-dichlorobenzene, TT–T–DCI showed improved solubility in $CHCl_3$ and *o*-dichlorobenzene. In contrast, TT–FT–DCI possesses a high solubility of >10 mg mL^{-1} owing to the combination of spiro-substituted fluorene units with branched 2-ethylhexyl chains. Therefore, in the following section, we use TT–FT–DCI and TT–T–DCI.

First, we investigated the thermal properties of TT–FT–DCI and TT–T–DCI (Fig. S2†). Thermogravimetric analysis (TGA) under a N_2 atmosphere showed no significant weight loss of either compound up to 300 °C, and 5% weight loss was observed at 328 and 332 °C for TT–FT–DCI and TT–T–DCI, respectively. This result indicates that these molecules are thermally stable and can be used in OSCs. As a result of sweeping up to 300 °C by differential scanning calorimetry analysis, melting and crystallization peaks were observed at 265 °C and 200 °C for TT–T–DCI. In contrast, TT–FT–DCI showed a gentle heat capacity shift with no clear peak. These results indicate that TT–T–DCI possesses crystalline nature, whereas TT–FT–DCI is expected to form amorphous state in the solid state.

2.2. Computational studies

To understand the influence of the FT unit on the rigidity of the π-conjugated skeleton, potential energies against dihedral angles were estimated for TT–FT(m) and TT–T(m) using density functional theory (DFT) calculations at B3LYP with 6-31G(d,p) basis set. Note that we replaced all alkyl groups with methyl groups to reduce the computational load (denoted as FT(m) and T(m) for clarity). From each potential energies, probabilities (P) against dihedral angles were plotted based on the equation $P = \exp(-E_i/k_BT)$, where E_i, k_B, and T are the energy of the i metastable state, Boltzmann constant, and temperature, respectively (Fig. 2a).[60] Whereas TT–T(m) exhibited a broad probability between $\theta = 180°$ and 140°, TT–FT(m) has a relatively narrow distribution. This result indicates that the introduction of the FT unit contributes to suppressing the dynamic fluctuation.

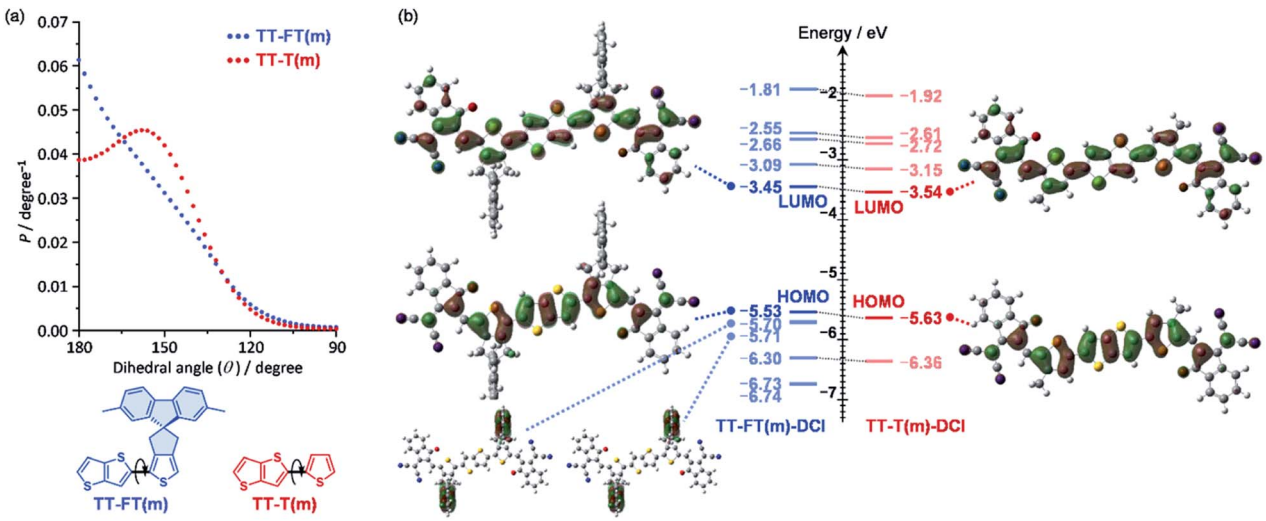

Fig. 2 (a) Probabilities against dihedral angles for TT–FT(m) and TT–T(m), and (b) molecular orbitals and their energy levels for TT–FT(m)–DCI and TT–T(m)–DCI.

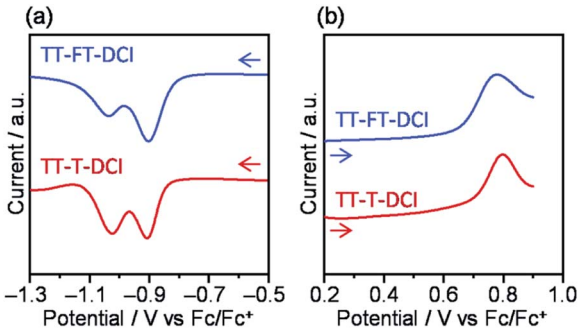

Fig. 3 Differential pulse voltammograms for (a) cathodic scans and (b) anodic scans.

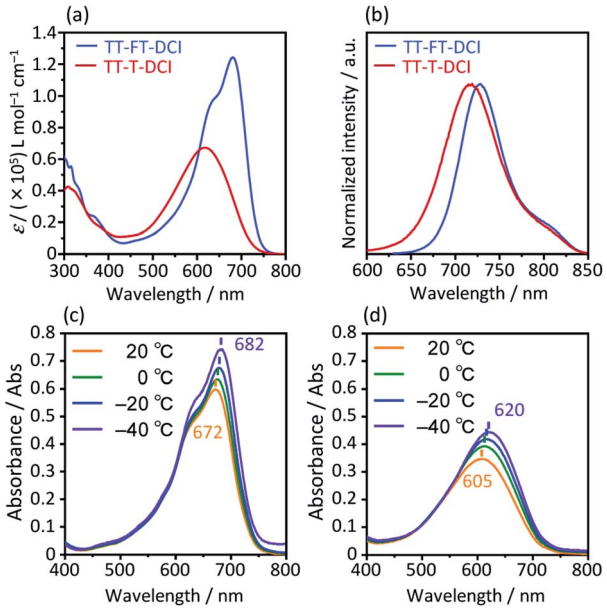

Fig. 4 UV-vis absorption spectra (a) and emission spectra (b) in $CHCl_3$ solutions. Temperature-dependent UV-vis absorption spectra for (c) TT–FT–DCI and (d) TT–T–DCI in dichloromethane.

We also optimized the model structures of TT–FT(m)–DCI and TT–T(m)-DCI (Fig. S3†). These results suggest that TT–FT–DCI and TT–T–DCI possess a planar π-conjugated skeleton. The spiro-flanked fluorene units in TT–FT(m)–DCI were aligned perpendicular to the main π-conjugated skeleton. This steric configuration is expected to suppress the π–π stacking interactions in the thin-film. The lowest unoccupied molecular orbitals (LUMOs) and highest occupied molecular orbitals (HOMOs) of TT–FT(m)–DCI and TT–T(m)–DCI are illustrated in Fig. 2b. These frontier orbitals are distributed throughout the π-conjugated main chain. Although no coefficients were present in the fluorene unit of TT–FT(m)–DCI, the molecular orbitals of the fluorene units were found at HOMO − 1 (−5.70 eV) and HOMO − 2 (−5.71 eV). The estimated LUMO and HOMO energy levels of these compounds were almost identical, and compounds with LUMO energy levels of approximately −3.5 eV were expected to function as acceptor materials.[9,10,13,14]

2.3. Electrochemical and photophysical properties

To investigate the electrochemical properties of TT–FT–DCI and TT–T–DCI, cyclic voltammetry (CV) and differential pulse voltammetry (DPV) were performed in dichloromethane (CH_2Cl_2) containing 0.1 M tetrabutylammonium hexafluorophosphate ($TBAPF_6$) as the supporting electrolyte, and the potentials were calibrated using a ferrocene/ferrocenium (Fc/Fc^+) redox couple as an internal standard. The voltammograms are shown in Fig. 3 and S4,† and the electrochemical data extracted from DPV are summarized in Table 1. Reversible oxidation and irreversible reduction waves were observed for both compounds in the CV measurements (Fig. S4†). From the oxidation peak in DPVs in Fig. 3b, the HOMO energy levels (E_{HOMO}) of TT–FT–DCI and TT–T–DCI were experimentally determined to be −5.71 and −5.75 eV, respectively.[61,62] Based on the first reduction peaks, the LUMO energy levels (E_{LUMO}) of TT–FT–DCI and TT–T–DCI were determined to be the identical value of −3.89 eV. The similar energy levels of TT–FT–DCI and TT–T–DCI indicate that the electronic perturbation of the spiro-substituted fluorene units against the π-conjugated framework is limited.

The electron affinity (E_A) and ionization potential (I_p) of the thin films were determined using low-energy inverse photoemission spectroscopy (LEIPS) and photoelectron yield spectroscopy (PYS) (Fig. S5†). The E_A value was found to be 3.78 eV below the vacuum level for both compounds. The I_p values were found to be 5.81 eV for TT–FT–DCI and 5.85 eV for TT–T–DCI. These estimated energy levels indicated that TT–FT–DCI and TT–T–DCI can function as acceptors when combined with low-bandgap donor polymers in OSCs.[9,10,13,14]

The photophysical properties of TT–FT–DCI and TT–T–DCI were investigated using UV-vis absorption spectroscopy in a dilute $CHCl_3$ solution. As shown in Fig. 4a, while one absorption band with vibrational structure was observed for TT–FT–DCI, TT–T–DCI exhibited a broad structureless absorption band. Irrespective of the same π-conjugated framework,

Table 1 Physical properties of TT–FT–DCI and TT–T–DCI

Compound	E_{red}[a]/V	E_{ox}[a]/V	E_{LUMO}[b]/eV	E_{HOMO}[b]/eV	λ_{max} (sol.)[c]/nm	ε/L mol^{-1} cm^{-1}	λ_{max} (film)/nm	E_A[d]/eV	I_p[e]/eV
TT–FT–DCI	−0.91	0.91	−3.89	−5.71	680	1.24×10^5	653	3.78	5.81
TT–T–DCI	−0.91	0.95	−3.89	−5.75	617	0.67×10^5	739	3.78	5.85

[a] Determined by DPV. [b] Approximation from DPV for the Fc/Fc^+ level is −4.8 eV *vs.* vacuum. [c] In $CHCl_3$. [d] Determined by LEIPS. [e] Determined by PYS.

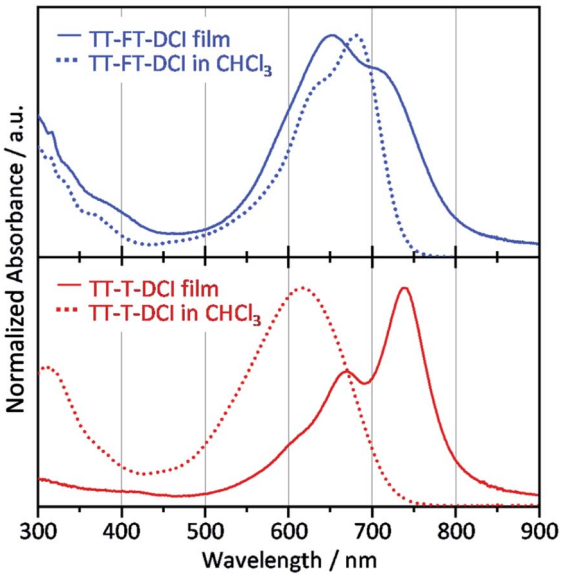

Fig. 5 UV-vis absorption spectra of films (solid lines) and in $CHCl_3$ solutions (dotted lines) for TT–FT–DCI and TT–T–DCI.

the maximum absorption wavelength (λ_{max}) of TT–FT–DCI at 680 nm was red-shifted by 63 nm compared to that of TT–T–DCI (617 nm). Furthermore, the full width at half-maximum (FWHM) of the absorption band of TT–FT–DCI (110 nm; 2600 cm^{-1}) is narrower than that of TT–T–DCI (146 nm; 4000 cm^{-1}), and the molar absorption coefficient (ε) of TT–FT–DCI is 1.8 times larger than that of TT–FT–DCI. The absorption spectra of TT–FT–DCI and TT–T–DCI showed no concentration dependence in the range of 0.2–50 μM (Fig. S6†), indicating that the observed difference between TT–FT–DCI and TT–T–DCI was not caused by intermolecular interactions. We also measured temperature-dependent absorption spectra. As shown in Fig. 4c and d, with decreasing temperature, the λ_{max} of TT–FT–DCI and TT–T–DCI red-shifted with increasing ε values. These results imply that the thermodynamic conformational probability has a significant influence on the photophysical properties. To support this hypothesis, time-dependent (TD) DFT calculations at the B3LYP/6-31G(d,p) level were performed for TT–FT(m)–DCI and TT–T(m)–DCI. In the case of the optimized planar structures, the corresponding transitions from HOMO to LUMO were predicted to be 710 nm with an oscillator strength (f) of 2.54 for TT–FT(m)–DCI and 700 nm with $f = 2.69$ for TT–T(m)–DCI. Since these calculated results did not reproduce the experimental phenomena well, we performed dihedral-dependent TD-DFT calculations to investigate the influence of planarity on the absorption spectra. As summarized in Fig. S7,† with a decreasing dihedral angle between thiophene and thienothiophene units from 180° to 90°, the calculated λ_{max} values were blue-shifted and the f values became smaller for both TT–FT(m)–DCI and TT–T(m)–DCI. Because the trend in the distorted structure agrees well with the absorption spectra of TT–T–DCI, we considered that TT–T–DCI can exhibit conformational flexibility in solutions. In contrast, the presence of cyclopentene-annelated thiophene in TT–FT–DCI is effective in forming a rigid structure, leading to a narrow probability of conformation and a relatively high ε value in solution. Fig. 4b shows the emission spectra of TT–FT–DCI and TT–T–DCI in a $CHCl_3$ solution. The maximum emission wavelengths were 728 nm for TT–FT–DCI and 719 nm for TT–T–DCI. In contrast to the absorption spectra, there was no significant difference in the maximum emission wavelengths of TT–T–DCI and TT–T–DCI. This result indicates that these molecules possess similar electronic structures in the excited states. From the λ_{max} and emission maxima, the Stokes shifts were calculated to be 970 cm^{-1} for TT–FT–DCI and 2300 cm^{-1} for TT–T–DCI. The relatively small Stokes shift of TT–FT–DCI supports improved molecular planarity.

Compared to the solution state, the TT–T–DCI film showed an apparent red shift of approximately 120 nm. This result was rationalized by the appearance of strong intermolecular interactions in the solid state (Fig. 5).[63,64] In contrast, a large overlap between the solution and thin-film spectra was observed for TT–FT–DCI, indicating that the presence of the FT unit disturbed the intermolecular interactions.[53] Owing to changes in the vibronic structures, the λ_{max} of TT–FT–DCI in the film was blue-shifted in comparison to that in the solution. The optical energy gaps (E_g^{opt}) of TT–FT–DCI and TT–T–DCI in the film state were calculated from the onset wavelength of the absorption spectra. E_g^{opt} was 1.58 eV for both the compounds.

X-ray diffraction (XRD) measurements were performed to investigate the molecular arrangement of the thin films (Fig. S8†). The pristine TT–FT–DCI thin-film showed very weak diffraction at $\theta = 4$–5° ($d = \sim 2$ nm) in the in-plane direction. This d-spacing roughly corresponded to the length of the molecular long-axis. Therefore, we considered that TT–FT–DCI mainly formed amorphous films with concomitant small crystal structures with face-on alignment. In contrast, for the TT–T–DCI thin-film, a clear diffraction peak was observed at 4.8° ($d =$ 1.8 nm) in the out-of-plane direction and 24.8° ($d = 0.36$ nm) in the in-plane direction. These d-spacings correspond to the long axis length and the general π–π stacking distance. Therefore, TT–T–DCI forms a crystalline structure with an edge-on alignment in the thin-film state. The observed bathochromic shift in the TT–T–DCI thin-film is in good agreement with the XRD results. We also considered that the narrow FWHM of the absorption band of TT–T–DCI in the film is due to the formation of an ordered structure.

2.4. OSC characteristics

The photovoltaic characteristics of TT–FT–DCI and TT–T–DCI as new acceptors were investigated using an inverted configuration of ITO/ZnO/PBDB-T[65] (CAS Registry No. 1415929-80-4):acceptor/MoO_3/Ag.[66] The details of the device fabrication condition are provided in the ESI.† The chemical structure of PBDB-T is presented in Fig. S1.† The active layers were optimized by screening the donor and acceptor ratios, process solvents, additives, concentrations, and rotational speeds (Tables S2 and S3†). The current density (J)–voltage (V) characteristics of the OSCs under AM 1.5 G solar irradiation (100 mW cm^{-2}) and the corresponding external quantum efficiency (EQE)

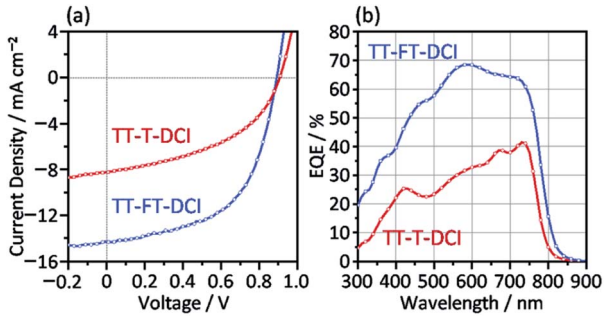

Fig. 6 (a) J–V curves and (b) EQE spectra for PBDB-T:TT–FT–DCI and PBDB-T:TT–T–DCI OSC devices.

spectra are shown in Fig. 6. The results for operational stability of these devices are shown in Fig. S9.† The representative device parameters of short-circuit current (J_{SC}), open-circuit voltage (V_{OC}), and fill factor (FF) are summarized in Table 2. The best PCEs of TT–FT–DCI and TT–T–DCI were 7.13 and 3.41%, respectively. Compared with those of the PBDB-T:TT–T–DCI device, the J_{SC} and FF of the PBDB-T:TT–FT–DCI-based device were improved. This result indicates that TT–FT–DCI has advantages for carrier dynamics from exciton formation to charge extraction in OSCs, which will be discussed in the following sections. The EQE measurements showed that the PBDB-T:TT–FT–DCI device recorded a maximum value (EQE_{max}) of 68% at 580 nm, whereas the PBDB-T:TT–T–DCI device showed an EQE_{max} of 41% at 730 nm. Fig. S10† shows the absorption spectra of the active layers formed on the quartz plates. Because the EQE responses around 500–650 and 600–750 nm were mainly attributable to PBDB-T and TT–FT–DCI, respectively, both the donor and acceptor contributed to the photocurrent generation. The difference in the V_{OC} values of PBDB-T:TT–FT–DCI and PBDB-T:TT–T–DCI devices was 0.02 V. From the onset wavelengths of the absorption spectra of the active layers, the E_g^{opt}(D:A) values of the PBDB-T:TT–FT–DCI and PBDB-T:TT–T–DCI blend films were estimated to be 1.57 eV (792 nm) and 1.59 eV (778 nm), respectively. From the equation $E_{loss} = E_g^{opt}(D:A) - eV_{OC}$,[67,68] the energy loss (E_{loss}) was calculated to be 0.68 eV for both the OSCs.

The surface morphologies of the PBDB-T:TT–FT–DCI and PBDB-T:TT–T–DCI blend films were investigated by atomic force microscopy (AFM). As illustrated in Fig. S11,† the PBDB-T:TT–FT–DCI films showed a more distinct grain structure with a mean square roughness (R_{rms}) of 2.1 nm, whereas the PBDB-T:TT–T–DCI films formed a smooth surface with an R_{rms} of 0.68 nm. The active layers were also investigated using transmission electron microscopy (TEM). As shown in Fig. S12,† the films did not show any significant macroscopic ordered structures, indicating that both PBDB-T:TT–FT–DCI and PBDB-T:TT–T–DCI blend films form homogeneous active layers.

To investigate the crystallinity and molecular arrangement of the PBDB-T:TT–FT–DCI and PBDB-T:TT–T–DCI films, XRD measurements were performed. As shown in Fig. S8,† the crystallinity of the blend films resembled that of the acceptor pristine films. The PBDB-T:TT–T–DCI film exhibited distinct diffraction based on TT–T–DCI, whereas the PBDB-T:TT–FT–DCI film showed a very weak diffraction peak at $\theta = 4.4°$ in the out-of-plane direction attributed to TT–FT–DCI.

To estimate the macroscopic hole and electron mobilities, the space-charge limited current (SCLC) of blended films were investigated using ITO/PEDOT:PSS/PBDB-T:acceptor/MoO_3/Ag for hole-only devices and ITO/ZnO/PBDB-T:acceptor/Ca/Al for electron-only devices.[69–71] The J–V and J–V^2d^{-3} plots are shown in Fig. S13,† and the estimated hole mobilities (μ_h) and electron mobilities (μ_e) are listed in Table 2. The hole transport attributed to PBDB-T exhibited the same order of magnitude of μ_h in both blend films. In contrast, the μ_e value of the PBDB-T:TT–FT–DCI films was two orders of magnitude higher than that of the PBDB-T:TT–T–DCI films. This result indicates that TT–FT–DCI has an aptitude for electron transport in OSCs, and the balanced μ_h and μ_e of the PBDB-T:TT–FT–DCI blend film is considered to contribute to the higher FF of the OSCs.[72–75] The edge-on orientation of TT–T–DCI in the PBDB-T:TT–T–DCI film, which was observed in the XRD results (Fig. S8†), is disadvantageous for the electron transport.

2.5. Time-resolved UV-vis and infrared absorption spectroscopy

Picosecond transient absorption (TA) measurements were performed to understand the photoinduced responses of TT–FT–DCI and TT–T–DCI. As shown in Fig. S14a and b,† broad absorption was observed at approximately 990 nm for both neat TT–FT–DCI and TT–T–DCI films by 730 nm laser pulse irradiation. This absorption was assigned to the singlet excited state (S_1), and the lifetime of S_1 of TT–FT–DCI was longer than that of the TT–T–DCI films, as shown in Fig. 7a.

To further investigate the photoexcited dynamics of TT–FT–DCI and TT–T–DCI, changes in the vibrational frequency of the CN group were observed using time-resolved IR (TR-IR) absorption spectroscopy. This method is useful for observing the changes in the electronic and molecular structures induced

Table 2 OSC characteristics of optimized devices and electron and hole mobilities of blend films

Acceptor	J_{SC}[a]/mA cm^{-2}	V_{OC}[a]/V	FF[a]/%	PCE[a,b]/%	R_{sh}[c]/Ω cm^2	R_s[c]/Ω cm^2	EQE_{max}/%	μ_e[d]/cm^2 V^{-1} s^{-1}	μ_h[e]/cm^2 V^{-1} s^{-1}
TT–FT–DCI	14.30	0.89	56	7.13 (7.02 ± 0.11)	7.7×10^4	6	68	1.3×10^{-6}	7.7×10^{-6}
TT–T–DCI	8.22	0.91	46	3.41 (3.08 ± 0.20)	5.5×10^2	35	41	9.4×10^{-8}	3.3×10^{-6}

[a] ITO/ZnO/PBDB-T:acceptor/MoO_3/Ag. [b] The average and standard deviation of 5 devices are provided in parentheses, see the ESI for details. [c] Shunt resistance (R_{sh}) and series resistance (R_s) were estimated from J–V curves on Fig. S6b. [d] ITO/ZnO/PBDB-T:acceptor/Ca/Al. [e] ITO/PEDOT:PSS/PBDB-T:acceptor/MoO_3/Ag.

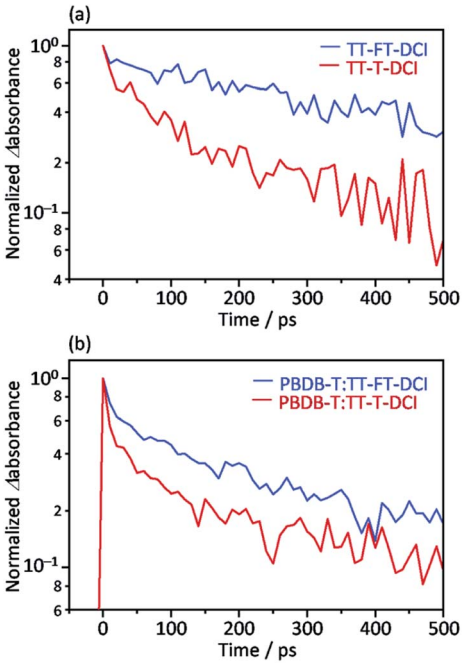

Fig. 7 Time profile of the transient absorption at 990 nm for (a) TT–FT–DCI and TT–T–DCI neat films and (b) PBDB-T:TT–FT–DCI and PBDB-T:TT–T–DCI blend films.

by photoirradiation because the vibrational frequencies are very sensitive to the changes in the charge densities around the chemical bonds.[76,77] When TT–FT–DCI was photoexcited, the TR-IR spectra of CN exhibited a bipolar shape with negative and positive peaks at 2225 and 2208 cm^{-1}, respectively (Fig. 8a and S16a†). This spectral change indicates that the vibrational frequency of CN observed at 2218 cm^{-1}, on the top of Fig. 8a, was red-shifted by photoexcitation, indicating that the density of electron around CN is increased. A similar red-shift was observed for TT–T–DCI, but an additional peak appeared at 2218 cm^{-1} (Fig. 8b). The peak intensities at 2218 cm^{-1} and 2204 cm^{-1} decreased remarkably and increased immediately after excitation. This is in contrast to that of TT–FT–DCI, which is almost constant within a few ps. The decrease of 2218 cm^{-1} TA and the increase of 2204 cm^{-1} TA of TT–T–DCI shown in Fig. S16b† are well correlated, indicating that some electronic and/or structural changes occurred within a few picoseconds. A possible reason for the few-picosecond TR-IR signal is the conformational relaxation of the TT–T–DCI molecular structure. One of the reasons for this conformational change is the torsional motion of the π-conjugated skeleton from a nonplanar to planar configuration. The skeleton of TT–T–DCI is expected to be more flexible than that of TT–FT–DCI; therefore, it is likely to deviate slightly from the planar structure in the film. After photoexcitation, the structure of TT–T–DCI can relax to a more planar conformation within picoseconds.[78,79] In contrast, such conformational changes would be limited for TT–FT–DCI because it has a more rigid structure than TT–T–DCI.

The same TA measurements were performed for the blend films of TT–FT–DCI and TT–T–DCI with PBDB-T. In this experiment, only the acceptor molecules (TT–FT–DCI or TT–T–DCI) were excited using 730 nm laser pulses. As shown in Fig. S15a and b,† a broad absorption was also observed at

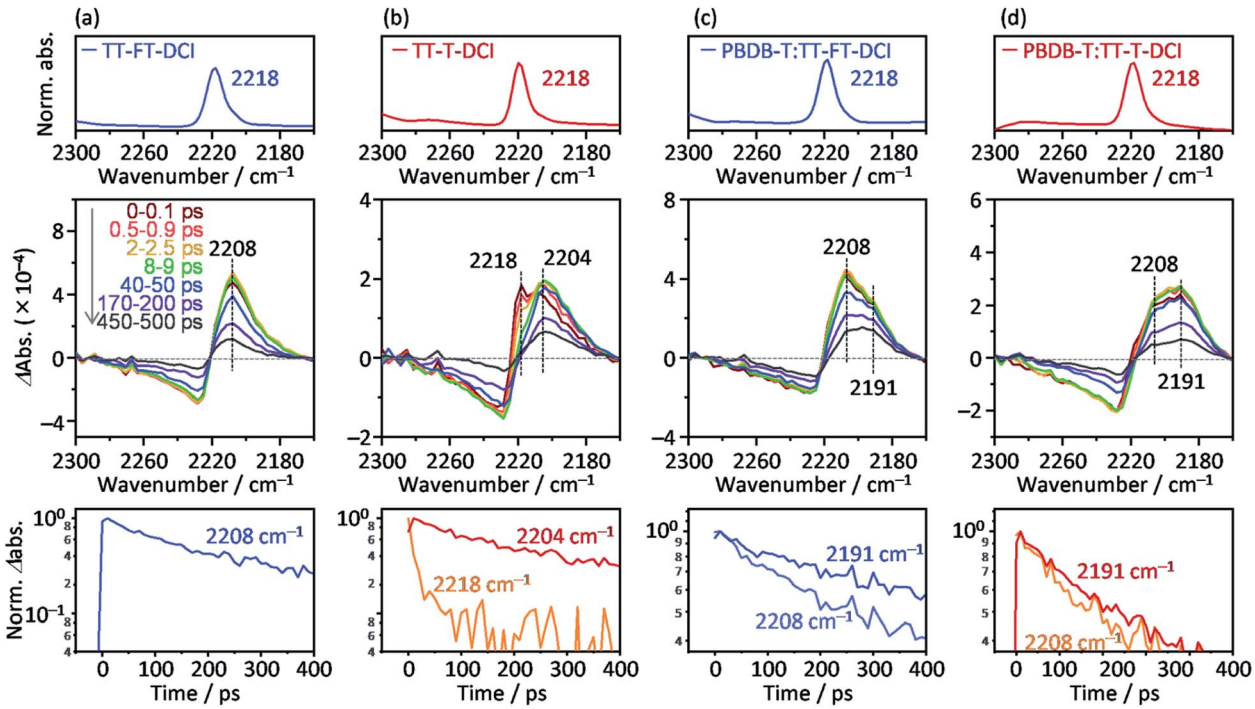

Fig. 8 Steady state absorption (top), transient absorption (middle), and temporal profiles of the transient absorption (bottom) in the near-infrared region for (a) TT–FT–DCI neat film, (b) TT–T–DCI neat film, (c) PBDB-T:TT–FT–DCI blend film, and (d) PBDB-T:TT–T–DCI blend film.

approximately 990 nm for both PBDB-T:TT–FT–DCI and PBDB-T:TT–T–DCI films, which are assigned to S_1 and/or the radical anion of TT–FT–DCI or TT–T–DCI. As in the case of the blend films, the lifetime of the charged species in PBDB-T:TT–FT–DCI was longer than that in PBDB-T:TT–T–DCI (Fig. 7b).

To further understand the electronic re-distribution processes in PBDB-T:TT–FT–DCI and PBDB-T:TT–T–DCI, the frequency shift of CN was observed using TR-IR spectroscopy. In the case of PBDB-T:TT–FT–DCI (Fig. 8c), two positive peaks appeared at approximately 2208 and 2191 cm^{-1}. The former was also observed in the neat TT–FT–DCI film (Fig. 8a), but the latter was absent in the neat TT–FT–DCI film. This result shows that the electron density around the CN of TT–FT–DCI was further increased in the presence of PBDB-T, indicating hole transfer from TT–FT–DCI to PBDB-T after exciton diffusion to the donor/acceptor interfaces. It is noted that the decay of the peak intensity at 2208 cm^{-1} (time constant $\tau = 386 \pm 14$ ps) was remarkably faster than that at 2191 cm^{-1} ($\tau = 705 \pm 27$ ps, bottom of Fig. 8c). This result indicates that the lifetime of holes located in PBDB-T is longer than that in TT–FT–DCI owing to hole transfer from TT–FT–DCI to PBDB-T and/or recombination of electrons and holes in the TT–FT–DCI domain.

In the case of PBDB-T:TT–T–DCI, two positive peaks appeared at 2208 and 2191 cm^{-1}, similar to the case of PBDB-T:TT–FT–DCI. However, the peak intensity at 2208 cm^{-1} is much smaller than that at 2191 cm^{-1} even at 0–0.1 ps (Fig. 8d). Furthermore, the decay rate of the peak intensity at 2208 cm^{-1} ($\tau = 304 \pm 14$ ps) was similar to that at 2191 cm^{-1} ($\tau = 341 \pm 9$ ps, bottom of Fig. 8d), which is in contrast to the case of PBDB-T:TT–FT–DCI. This indicates that the hole transfer from TT–T–DCI to PBDB-T is completed in hundreds of picoseconds region. These results show that the hole transfer from TT–T–DCI to PBDB-T occurs more rapidly and effectively than in PBDB-T:TT–FT–DCI because the TT–T–DCI domain is closely packed with a crystalline nature in contrast to the TT–FT–DCI domain with an amorphous nature. However, the band intensity of 2191 cm^{-1} in PBDB-T:TT–FT–DCI decayed remarkably slower than that in PBDB-T:TT–T–DCI (Fig. S17†), whereas the 2208 cm^{-1} band intensity decayed rapidly, indicating that the hole transfer proceeded from TT–FT–DCI *via* extensive exciton diffusion during the long survival time (705 ps from 2208 cm^{-1} decay of Fig. 8c) of the exciton and that the lifetime of holes in PBDB-T:TT–FT–DCI was longer than that of holes PBDB-T:TT–T–DCI. This result could be accounted for by considering the electron mobility (Table 2): the electron mobility of TT–FT–DCI is larger than that of TT–T–DCI. Hence, the electrons in TT–FT–DCI can easily move away from the holes, resulting in the suppression of recombination. These slower deactivation processes in TT–FT–DCI are responsible for the superior solar cell performance compared to that of TT–T–DCI.

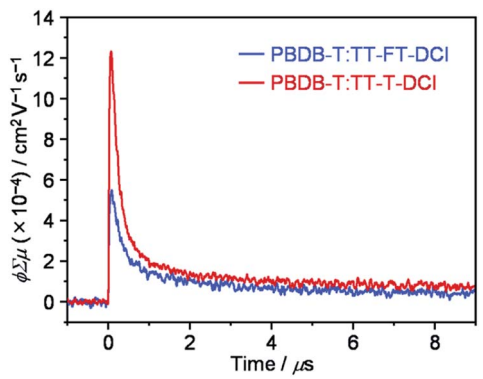

Fig. 9 FP-TRMC transient of PBDB-T:TT–FT–DCI and PBDB-T:TT–T–DCI blend films.

2.6. Time-resolved microwave conductivity

To investigate the lifetimes of free carriers in PBDB-T:TT–FT–DCI and PBDB-T:TT–T–DCI blend films, FP-TRMC measurements were performed.[80] As shown in Fig. 9, the transient photoconductivity ($\phi\Sigma\mu$) of the PBDB-T:TT–FT–DCI blend displays the maximum $\phi\Sigma\mu_{max}$ of 5.5×10^{-4} cm^2 V^{-1} s^{-1}, where ϕ and $\Sigma\mu$ represent the charge carrier generation yield and the sum of the hole and electron mobilities, respectively.[80] The $\phi\Sigma\mu_{max}$ of the PBDB-T:TT–T–DCI blend was found to be 1.2×10^{-3} cm^2 V^{-1} s^{-1}. Therefore, it was suggested that the PBDB-T:TT–T–DCI blend film shows a higher local mobility associated with a more substantial self-assembling nature than PBDB-T:TT–FT–DCI, as evident from the UV-vis absorption spectra in Fig. 5 and the XRD data in Fig. S8.†

Based on TA, TR-IR, and FP-TRMC measurements, it is indicated that TT–FT–DCI possesses a longer lifetime for the S_1 and charge-transfer (CT) state, as well as for the charge-separation (CS) state, than TT–T–DCI. The longer lifetimes of these transient species are expected to facilitate photocarrier generation in OSCs, which rationalizes the high J_{SC} and shunt resistance (R_{sh}) of the PBDB-T:TT–FT–DCI based OSCs.

2.7. Time-resolved electron paramagnetic resonance

2.7.1 Photoinduced CS state geometry in PBDB-T:TT–FT–DCI blend films. To examine the molecular conformations and geometries of the photoinduced charge-separated state, TREPR measurements were performed on the substrate/ZnO/PBDB-P:TT–FT–DCI blend films for three different field directions obtained by 532 nm pulsed laser irradiation at 80 K (Fig. 10), exhibiting electron spin polarization (ESP) by the microwave absorption (*A*) and emission (*E*). The thin films were cut into seven pieces of ~4 mm × 20 mm and were inserted into the EPR sample tubes with 5 mm OD (left and middle of Fig. 10d) as multilayered films. Thus, one can align the direction of the magnetic field B_0 with respect to the normal vector (n) from the substrates (as indicated by the arrows in the middle of Fig. 10d). We also prepared small cut films inserted into the EPR tube as a powder-like sample (Fig. 10d). An identical TREPR spectrum was obtained using a selecting the longer excitation wavelength of 710 nm (Fig. S18†), which predominantly pumped the acceptor. The emissive signal in the *E*/*A* polarization spectra corresponds to the resonance by the reduced NFA (TT–FT–$DCI^{-\bullet}$: $g \approx 2.004$), while the absorptive polarization corresponds to the resonance line by the oxidized PBDB-T (PBDB-$T^{+\bullet}$: $g \approx 2.003$), indicating that the photoinduced CS states[81] were

observed at 0.5 μs after the laser irradiations. Surprisingly, the emissive spectrum shape was dependent on the field direction with respect to the *n* vector from the substate, indicating that the conformation of TT–FT–DCI$^{-\bullet}$ is not randomly distributed in the CS state. In Fig. 10a, the emissive signal was broadened around the lower field region, as indicated by the arrow, while the *E* signal in Fig. 10b was shifted toward the higher field side constituting the sharp *E*/*A* polarization pattern.[71] This is explained by considering the anisotropies in the *g*-factor (g_x = 2.0047, g_y = 2.0033, and g_z = 2.0020) and in the hyperfine couplings based on the molecular orbital calculation using the ORCA program package, version 5.0.2, for TT–FT–DCI$^{-\bullet}$ as detailed in the ESI.† To obtain details of the molecular conformations of the CS state, we computed the spin-polarized EPR spectra from the singlet-precursor spin-correlated radical pair (SCRP)[82,83] model using MATLAB code with parameters of the exchange coupling (J = 85 μT) and the spin–spin dipolar coupling (D = −320 μT). The results showed the inter-spin separation (r) of 2.1 nm between the electron and hole by the point-dipole approximation from the red fitting lines in Fig. 10. The computation method[84] and EPR parameters[85] (Table S7 and Fig. S19) are detailed in the ESI.† As a result, the broad lower field emissive signal in Fig. 10a was explained by the contributions from g_x = 2.0047 and g_y = 2.0033 of TT–FT–DCI$^{-\bullet}$, while the sharp emissive component in (b) was explained by g_z = 2.0020 at the higher field contributed by the *g*-factor close to the free electron. This implies that the normal vector by g_z from the aromatic plane in TT–FT–DCI$^{-\bullet}$ is parallel to the *n* vector, and the CS state takes on the face-on conformation ($\theta_n = 0° \pm 10°$ for the g_z axis) nearby the ZnO/active layer interface. We also examined the molecular conformations of excitons by TREPR measurements for both the TT–FT–DCI pristine films and blend samples at 80 K. The face-on conformation of the CS state was highly distinguishable from the conformations of the triplet excitons, as described in the ESI (Fig. S20–S23).†[86,87]

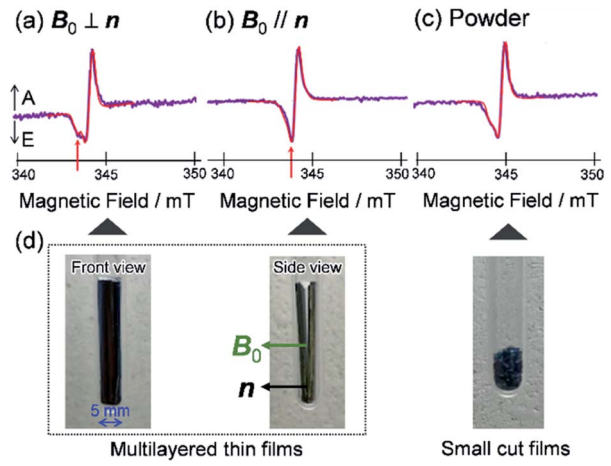

Fig. 10 TREPR spectroscopy of PBDB-T:TT–FT–DCI blend film. TREPR spectra of the photoinduced CS states observed for (a) $B_0 \perp n$, (b) $B_0 \parallel n$ and (c) small cut films, respectively. B_0 and n represent the magnetic field and the normal vector from the film substrate. (d) Photos of the thin films with front view, side view and numbers of cut films.

To visualize conformations of the CS state, we mapped (Fig. 11a) the electron spin polarization (*i.e.* the transverse magnetization at a field position indicated by the arrow in Fig. 10a) to all the field directions obtained from the fittings of the TREPR spectra.[84] A grazing-incidence wide-angle X-ray scattering study[88] of the ITO/ZnO/PBDB-T:ITIC blend film reported that PBDB-T polymers took on the face-on structures toward the out-of-substate direction, while the ITIC molecules tended to be disordered by the blend when 0.5% DIO additive was present. Based on this, it is very likely that the face-on character of TT–FT–DCI$^{-\bullet}$ in the CS state reflects the π–π stackings between TT–FT–DCI and PBDB-T (Fig. S8f†), which directly interacts with the ZnO surface, as shown by the aromatic molecule underneath the ZnO surface in Fig. 11b. From the above discussion with $\theta_n = 0° \pm 10°$, one can obtain a geometric model of the CS state, as shown in Fig. 11b, when the principal axis systems are considered as shown in Fig. 11c and d. Notably, a direct face-on interaction between the TT–FT–DCI aromatic plane and the ZnO surface is unlikely at θ_n = 0° because of the steric hindrance by the spiro-fluorene groups substituted in the acceptor. This is consistent with the tilted conformation of the triplet exciton shown in Fig. S21d and S22c.† Additionally, the face-on situations of the donor interacting with the cathode (Fig. 11b) may hinder the electron injection through insulating LUMOs of the donors, resulting in the trapped CS states following the initial singlet exciton migration toward the ZnO surface regions and subsequent charge separations, as was characterized to be the trapped triplet excitons in the pristine films of the disordered environments (Fig. S18†). The present trap characteristics of the CS state were supported by observations of Rabi oscillation[81] at a microwave power of 2.5 mW (Fig. S23†).

Thus, it is conceived that the present CS states are generated as a result of long-range exciton diffusions within the nanosecond survival time (705 ps from the 2208 cm^{-1} decay of Fig. 8c) in the vicinity of the ZnO surface, causing the trap characteristics *via* the dielectric response from ZnO, which possesses a higher dielectric constant[89] ($\varepsilon_s \approx 8$) than organic semiconductors. Based on the exciton diffusion coefficients (D_{ex} = 10^{-2} cm^2 s^{-1}) of the related NFA films,[90] the exciton diffusion length was estimated to be $L_D = \sqrt{6D_{ex}\tau} \approx 80$ nm when τ = 1 ns is substituted as the present survival time of the exciton. This coincides well with the width (120 nm) of the photoactive layer, suggesting that ultimate distant charge separations dominantly occur around the ZnO surface area following long-range exciton-diffusion. This is also consistent with a previous report that showed that the molar ratio of NFA molecules is larger at the ZnO surface than that of the donor.[88]

In addition to the spin-polarized CS states, second-lived trapped radical species were also observed using steady-state EPR spectroscopy under field modulations during 532 nm laser irradiations at 80 K (Fig. S24 and S25†). However, the *E*/*A* polarized SCRP spectrum in Fig. 11b is absent at room temperature (Fig. S26†), indicating that the shorter-lived SCRP was de-trapped and thus contributed to the photocurrent, because the distance between the charges was sufficiently long

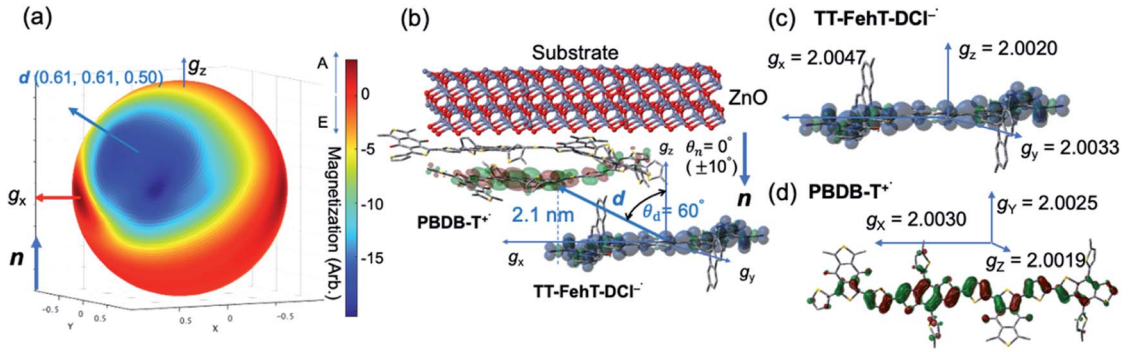

Fig. 11 Geometries of the photoinduced charge separated state. (a) Electron spin polarization imaging map of the transverse magnetization showing the direction ($\theta_d = 60°$, $\phi_d = 45°$) of the inter-spin vector $d = (0.61, 0.61, 0.50)$ from the electron to the hole in the g_x–g_y–g_z axis system in TT–FT–DCI$^{-\bullet}$. (b) Conformation model of the CS state with respect to the substrate normal vector. (c and d) Principal axes and values of the g-tensors.

(r = 2.1 nm). More details on the trap characteristics and the effects of exciton diffusion are described in Fig. S25–S27.†

In our previous study, we showed that the face-on orientations of acceptors against the aromatic planes of donors at the interfaces are advantageous for charge separation.[91,92] Therefore, to investigate the optimized stacking structure of PBDB-T and TT–FT–DCI, TT–FT(m)–DCI was placed on top of a model substructure of PBDB-T in a face-on conformation at a distance, and the structural optimization was performed by a DFT method with B3LYP-D3/6-31G(d,p) using Gaussian 16.[93] As a result, the bimolecular model converged to a stacking geometry with the distance between π-conjugated planes approaching approximately 4.3 Å (Fig. 12). TD-DFT calculations were carried out to estimate the optical transitions of the PBDB-T:TT–FT(m)–DCI complex, which showed transitions attributed to the CT transition between 750 and 900 nm (Fig. S28†). These CT transitions shifted to longer wavelengths compared with the corresponding transitions from pristine PBDB-T and TT–FT(m)–DCI. These calculated results reproduced the experimental results well: the absorption spectrum of the PBDB-T:TT–FT–DCI blend film showed a broad absorption band around 750 nm (Fig. S10(a) (top)†), which is red-shifted compared to that of the pristine TT–FT–DCI film (700–730 nm) (Fig. S10a (bottom)†). We considered that this band is partially attributed to the transition from the PBDB-T:TT–FT–DCI complex. Thus, the electrons and holes can also be separated *via* the CT states in PBDB-T:TT–FT–DCI to generate the distant CS states.

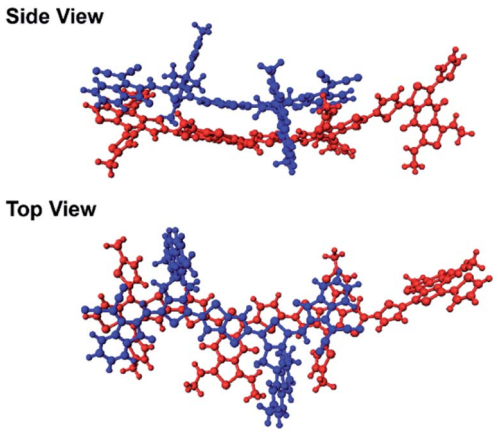

Fig. 12 Optimized geometries of the model complex of PBDB-T (red) and TT–FT(m)–DCI (blue).

2.7.2 EPR spectra of blend films employing TT–T–DCI acceptors. We further observed the TREPR spectra of the PBDB-T:TT–T–DCI blend film, which exhibited a lower solar cell performance (PCE = 3.41%) than the PBDB-T:TT–FT–DCI blend film with PCE = 7.13% (Fig. S29†). Although the *E*/*A* polarized TREPR spectra were observed, probably due to the long-range CS state in the PBDB-T:TT–T–DCI blend film, the triplet exciton signal contributions were predominant as opposed to the minor triplet generation in the PBDB-T:TT–FT–DCI blend film. This indicates that fewer electrons and holes were generated because of the lack of donor/acceptor miscibility originating from the excessive segregation and over-crystallization of the acceptor molecules nearby the cathode area when the spiro-fluorene group substitutions were absent. This was also confirmed by comparing the TREPR intensities between the substrate/ZnO/PBDB-P:TT–T–DCI and the TT–T–DCI pristine film at 80 K by 532 nm irradiation for the number of cut films (Fig. S30†).

The second-lived radical signals were also compared between the blend samples employing different acceptor molecules using steady-state EPR during 532 nm laser irradiations at 80 K (Fig. S31†). From the EPR intensities, the amount of accumulated charge was evaluated to be 2.6 times higher in the PBDB-T:TT–FT–DCI blend film than in PBDB-P:TT–T–DCI. Interestingly, this difference agrees well with the short-circuit current densities (J_{SC} = 14.30 mA cm^{-2} in PBDB-T:TT–FT–DCI *vs.* J_{SC} = 8.22 mA cm^{-2} in PBDB-T:TT–T–DCI) of the solar cells. Thus, it is concluded that the well-separated charges, including the transient CS states (Fig. 11b) at 80 K, can be de-trapped to contribute to the photocurrent densities for device performance at room temperature.

2.7.3 Mechanistic details of the photoinduced charge separations and subsequent electron injections. Previously, heterogeneous photoinduced charge-separation geometries

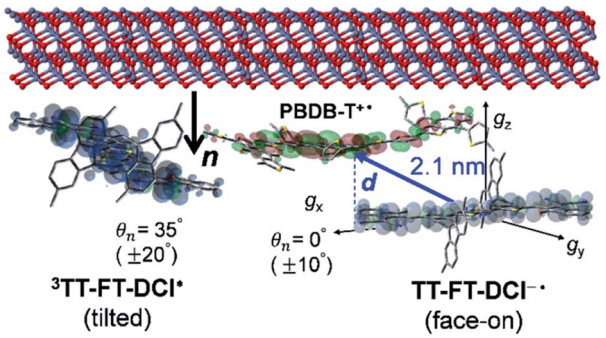

Fig. 13 Molecular orientations of the triplet exciton and the reduced radical in the CS state in the PBDB-T:TT–FT–DCI blend film.

were characterized in P3HT:$PC_{60}BM$ blend films using the TREPR method under cryogenic conditions.[81] The shallow trap characteristics of the 1.7 nm-separated radical pairs were reported to possess geometries with $\theta_d \approx 45°$ and $\phi_d \approx 35°$ which resembled the molecular conformations of the present results (Fig. 11b). Such distant CS states were reported to be generated by entropy enhancements *via* the electron–phonon (EP) couplings originating from the low-frequency vibrations mainly at the polymer crystalline regions.[94–96] In this regard, it can be proposed that the local face-on PBDB-T π–π stackings nearby the ZnO surface promote EP coupling, causing entropy enhancement to overcome the Coulomb attraction potential in Fig. 11b. The involvement of the EP effect and the shallow trap characteristics are consistent with the disappearance of the *E*/*A* polarized CS signals at elevated temperatures (Fig. S26†).

More importantly, the present locally ordered CS state conformation nearby the cathode is the highlight of the highly disordered morphology in view of whole photoactive layers employing the spiro-fluorene substitutions. Not only the homogeneous donor/acceptor miscibility for the efficient exciton migrations and subsequent charge generations as characterized by the long survival times in Fig. 8c, the local face-on conformation at the cathode side is a key to certainly inject the electrons for $\mu_e \ll \mu_h$ in Table 2 with preventions of the electron–hole recombination to conduct the superior PCE and V_{OC} values. In this respect, the direct interaction between the tilted π-orbital of acceptor and the ZnO surface (Fig. 13) is a crucial gateway for efficient electron injection when the triplet exciton trapping is absent under solar-irradiation. This is consistent with the larger μ_e of the OSC employing the TT–FT–DCI than that of the OSC with the TT–T–DCI acceptor.

3 Conclusion

In summary, to investigate the effects of rigid and sterically bulky structures of non-fused NFAs on transient photon-to-current dynamics, a new electron-accepting π-conjugated molecule, TT–FT–DCI, was developed. Theoretical calculations and photophysical measurements indicated that the introduction of the FT unit was effective for the rigidification of the π-conjugated framework. The J_{SC} and FF of the PBDB-T:TT–FT–DCI-based OSCs were significantly improved compared to those of PBDB-T:TT–T–DCI-based OSCs, achieving a maximum PCE of 7.13%. Time-resolved IR absorption spectroscopy of the pristine thin-films revealed that TT–FT–DCI exhibited smaller conformational relaxation than TT–T–DCI under photoexcitation conditions, which primarily originates from the rigid π-conjugated framework of TT–FT–DCI. Furthermore, TT–FT–DCI showed longer lifetimes of the excited and charge-separated states in the blend films than TT–T–DCI. For FP-TRMC measurements, a longer lifetime of free carriers was observed for the PBDB-T:TT–FT–DCI film. Time-resolved EPR measurements revealed that the CS state of PBDB-T:TT–FT–DCI adopted a face-on conformation near the ZnO electrode. This orientation is rationalized by the suppression of aggregation between the TT–FT–DCI molecules due to the presence of sterically bulky spiro-substituted fluorene units. We demonstrated that the rigid and sterically bulky structure of non-fused NFA has advantages in the dynamic process of photon-to-current conversion in the active layer of OSCs, which provides important insights into the material design for high-performance non-fused NFAs as well as deep understanding of solar cell operating mechanisms.

Conflicts of interest

There are no conflicts to declare.

Acknowledgements

This work was supported by JSPS KAKENHI (20H02814, 20K21224, 20H05841, 20KK0123, 19K15505, 20H04639, 20K15352, 21H05406, 20H05838, 19H00888, and 20K21174), CREST (J205101030), NEDO (21500248-0), and "Dynamic Alliance for Open Innovation Bridging Human, Environmental and Materials" from the Ministry of Education, Culture, Sports, Science and Technology, Japan. We are thankful to Nanotechnology Open Facilities, Osaka University (JPMXP09S21OS0010) for PYS measurements. We are also thankful to the Thermal & Electric Energy Technology Inc. Thanks are extended to the CAC, SANKEN, for assistance in obtaining elemental analyses and high-resolution mass spectra. Theoretical calculations for the dimer model were performed at Research Center for Computational Science in the Institute for Molecular Science (IMS) in Okazaki, Japan.

Notes and references

1 A. Polman, M. Knight, E. C. Garnett, B. Ehrler and W. C. Sinke, *Science*, 2016, **352**, aad4424.
2 C. Yan, S. Barlow, Z. Wang, H. Yan, A. K.-Y. Jen, S. R. Marder and X. Zhan, *Nat. Rev. Mater.*, 2018, **3**, 18003.
3 P. Cheng, G. Li, X. Zhan and Y. Yang, *Nat. Photonics*, 2018, **12**, 131–142.
4 J. Zhang, H. S. Tan, X. Guo, A. Facchetti and H. Yan, *Nat. Energy*, 2018, **3**, 720–731.
5 O. Inganäs, *Adv. Mater.*, 2018, **30**, 1800388.
6 G. Yu, J. Gao, J. C. Hummelen, F. Wudl and A. J. Heeger, *Science*, 1995, **270**, 1789–1791.

7 J. J. M. Halls, K. Pichler, R. H. Friend, S. C. Moratti and A. B. Holmes, *Appl. Phys. Lett.*, 1996, **68**, 3120–3122.
8 G. Zhang, J. Zhao, P. C. Y. Chow, K. Jiang, J. Zhang, Z. Zhu, J. Zhang, F. Huang and H. Yan, *Chem. Rev.*, 2018, **118**, 3447–3507.
9 A. Wadsworth, M. Moser, A. Marks, M. S. Little, N. Gasparini, C. J. Brabec, D. Baran and I. McCulloch, *Chem. Soc. Rev.*, 2019, **48**, 1596–1625.
10 C. B. Nielsen, S. Holiday, H.-Y. Chen, S. J. Cryer and I. McCulloch, *Acc. Chem. Res.*, 2015, **48**, 2803–2812.
11 S. Chatterjee, S. Jinnai and Y. Ie, *J. Mater. Chem. A*, 2021, **9**, 18857–18886.
12 D. Luo, W. Jang, D. D. Babu, M. S. Kim, D. H. Wang and A. K. K. Kyaw, *J. Mater. Chem. A*, 2022, **10**, 3255–3295.
13 D. Li, X. Zhang, D. Liu and T. Wang, *J. Mater. Chem. A*, 2020, **8**, 15607–15619.
14 Q. Yue, W. Liu and X. Zhu, *J. Am. Chem. Soc.*, 2020, **142**, 11613–11628.
15 C. Xu, Z. Zhao, K. Yang, L. Niu, X. Ma, Z. Zhou, X. Zhang and F. Zhang, *J. Mater. Chem. A*, 2022, **10**, 6291–6329.
16 X. Wang, Q. Sun, J. Gao, J. Wang, C. Xu, X. Ma and F. Zhang, *Energies*, 2021, **14**, 4200.
17 Y. Lin, J. Wang, Z. G. Zhang, H. Bai, Y. Li, D. Zhu and X. Zhan, *Adv. Mater.*, 2015, **27**, 1170–1174.
18 W. Zhao, D. Qian, S. Zhang, S. Li, O. Inganäs, F. Gao and J. Hou, *Adv. Mater.*, 2016, **28**, 4734–4739.
19 J. Yuan, Y. Zhang, L. Zhou, G. Zhang, H.-L. Yip, T.-K. Lau, X. Lu, C. Zhu, H. Peng, P. A. Johnson, M. Leclerc, Y. Cao, J. Ulanski, Y. Li and Y. Zou, *Joule*, 2019, **3**, 1140–1151.
20 L. Zhan, S. Li, Y. Li, R. Sun, J. Min, Z. Bi, W. Ma, Z. Chen, G. Zhou, H. Zhu, M. Shi, L. Zuo and H. Chen, *Joule*, 2022, **6**, 662–675.
21 Y. Cui, Y. Xu, H. Yao, P. Bi, L. Hong, J. Zhang, Y. Zu, T. Zhang, J. Qin, J. Ren, Z. Chen, C. He, X. Hao, Z. Wei and J. Hou, *Adv. Mater.*, 2021, **33**, 2102420.
22 A. Karki, J. Vollbrecht, A. J. Gillett, S. S. Xiao, Y. Yang, Z. Peng, N. Schopp, A. L. Dixon, S. Yoon, M. Schrock, H. Ade, G. N. M. Reddy, R. H. Friend and T.-Q. Nguyen, *Energy Environ. Sci.*, 2020, **13**, 3679–3692.
23 J. Sun, Z. Zhang, X. Yin, J. Zhou, L. Yang, R. Geng, F. Zhang, R. Zhu, J. Yu and W. Tang, *J. Mater. Chem. A*, 2018, **6**, 2549–2554.
24 L.-M. Wang, Q. Li, S. Liu, Z. Cao, Y.-P. Cai, X. Jiao, H. Lai, W. Xie, X. Zhan and T. Zhu, *ACS Appl. Mater. Interfaces*, 2020, **12**, 24165–24173.
25 B. Kan, J. Zhang, F. Liu, X. Wan, C. Li, X. Ke, Y. Wang, H. Feng, Y. Zhang, G. Long, R. H. Friend, A. B. Bakulin and Y. Chen, *Adv. Mater.*, 2018, **30**, 1704904.
26 M. T. Sajjad, A. Ruseckas, L. K. Jagadamma, Y. Zhang and I. D. W. Samuel, *J. Mater. Chem. A*, 2020, **8**, 15687–15694.
27 Y. Zhong, M. Causa, G. J. Moore, P. Krauspe, B. Xiao, F. Günther, J. Kublitski, R. Shivhare, J. Benduhn, E. BarOr, S. Mukherjee, K. M. Yallum, J. Rehault, S. C. B. Mannsfeld, D. Neher, L. J. Richter, D. M. DeLongchamp, F. Ortmann, K. Vandewal, E. Zhou and N. Banerji, *Nat. Commun.*, 2020, **11**, 833.
28 W. Li, M. Chen, J. Cai, E. L. K. Spooner, H. Zhang, R. S. Gurney, D. Liu, Z. Xiao, D. G. Lidzey, L. Ding and T. Wang, *Joule*, 2019, **3**, 819–833.
29 G. Han, Y. Guo, X. Song, Y. Wang and Y. Yi, *J. Mater. Chem. C*, 2017, **5**, 4852–4857.
30 S. M. Swick, T. Gebraad, L. Jones, B. Fu, T. J. Aldrich, K. L. Kohlstedt, G. C. Schatz, A. Facchetti and T. J. Marks, *ChemPhysChem*, 2019, **20**, 2608–2626.
31 X. Zhang, H. Wang, D. Li, M. Chen, Y. Mao, B. Du, Y. Zhuang, W. Tan, W. Huang, Y. Zhao, D. Liu and T. Wang, *Macromolecules*, 2020, **53**, 3747–3755.
32 X. Song, P. Sun, D. Sun, Y. Xu, Y. Liu and W. Zhu, *Nano Energy*, 2022, **91**, 106678.
33 X. Song, K. Zhang, R. Guo, K. Sun, Z. Zhou, S. Huang, L. Huber, M. Reus, J. Zhou, M. Schwartzkopf, S. V. Roth, W. Liu, Y. Liu, W. Zhu and P. Müller-Buschbaum, *Adv. Mater.*, 2022, **34**, 2200907.
34 J. Kalowekamo and E. Baker, *Sol. Energy*, 2009, **83**, 1224–1231.
35 J. Min, Y. N. Luponosov, C. Cui, B. Kan, H. Chen, X. Wan, Y. Chen, S. A. Ponomarenko, Y. Li and C. J. Brabec, *Adv. Energy Mater.*, 2017, **7**, 1700465.
36 W. Yang, W. Wang, Y. Wang, R. Sun, J. Guo, H. Li, M. Shi, J. Guo, Y. Wu, T. Wang, G. Lu, C. J. Brabec, Y. Li and J. Min, *Joule*, 2021, **5**, 1209–1230.
37 Y. Gao, M. Cui, S. Qu, H. Zhao, Z. Shen, F. Tan, Y. Dong, C. Qin, Z. Wang, W. Zhang, Z. Wang and Y. Lei, *Small*, 2022, **18**, 2104623.
38 L. Ma, S. Zhang, J. Wang, Y. Xu and J. Hou, *Chem. Commun.*, 2020, **56**, 14337–14352.
39 S. Li, L. Zhang, F. Liu, J. Ren, M. Shi, C.-Z. Li, T. P. Russell and H. Chen, *Adv. Mater.*, 2018, **30**, 1705208.
40 S. Feng, M. Li, N. Tang, X. Wang, H. Huang, G. Ran, Y. Liu, Z. Xie, W. Zhang and Z. Bo, *ACS Appl. Mater. Interfaces*, 2020, **12**, 4638–4648.
41 S. Chatterjee, Y. Ie, T. Seo, T. Moriyama, G.-J. A. H. Wetzelaer, P. W. M. Blom and Y. Aso, *NPG Asia Mater.*, 2018, **10**, 1016–1028.
42 T. Duan, M. Babics, A. Seitkhan, Y. Firdaus, R.-Z. Liang, F. Cruciani, S. Liu, S. Lopatin and P. M. Beaujuge, *J. Mater. Chem. A*, 2018, **6**, 9368–9372.
43 K. J. Thorley and I. McCulloch, *J. Mater. Chem. C*, 2018, **6**, 12413–12421.
44 T.-J. Wen, Z. X. Liu, Z. Chen, J. D. Zhou, Z. Q. Shen, Y. Q. Xiao, X. H. Lu, Z. Q. Xie, H. M. Zhu, C.-Z. Li and H. Z. Chen, *Angew. Chem., Int. Ed.*, 2021, **60**, 12964–12970.
45 X. Wang, X. Cui, H. Lu, Y.-N. Chen, Y. Liu, Y. Zhou, C. Zhang, J. Song, C. Li, Z. Zhang and Z. Bo, *Org. Electron.*, 2021, **89**, 106029.
46 Z.-P. Yu, Z.-X. Liu, F.-X. Chen, R. Qin, T.-K. Lau, J.-L. Yin, X. Kong, X. Liu, M. Shi, C.-Z. Li and H. Chen, *Nat. Commun.*, 2019, **10**, 2152.
47 X. Li, Z. Xu, X. Guo, Q. Fan, M. Zhang and Y. Li, *Org. Electron.*, 2018, **58**, 133–138.
48 D. Luo, X. Lai, N. Zheng, C. Duan, Z. Wang, K. Wang and A. K. K. Kyaw, *Chem. Eng. J.*, 2021, **420**, 129768.

49 Y.-N. Chen, M. Li, Y. Wang, J. Wang, M. Zhang, Y. Zhou, J. Yang, Y. Liu, F. Liu, Z. Tang, Q. Bao and Z. Bo, *Angew. Chem., Int. Ed.*, 2020, **59**, 22714–22720.
50 L. Ma, S. Zhang, J. Zhu, J. Wang, J. Ren, J. Zhang and J. Hou, *Nat. Commun.*, 2021, **12**, 5093.
51 M. Yang, W. Wei, X. Zhou, Z. Wang and C. Duan, *Energy Mater.*, 2021, **1**, 100008.
52 Y. Ie, Y. Okamoto, T. Inoue, S. Tone, T. Seo, Y. Honda, S. Tanaka, S. K. Lee, T. Ohto, R. Yamada, H. Tada and Y. Aso, *J. Phys. Chem. Lett.*, 2019, **10**, 3197–3204.
53 Y. Ie, M. Endou, S. K. Lee, R. Yamada, H. Tada and Y. Aso, *Angew. Chem., Int. Ed.*, 2011, **50**, 11980–11984.
54 Y. Ie, Y. Okamoto, T. Inoue, T. Seo, T. Ohto, R. Yamada, H. Tada and Y. Aso, *J. Am. Chem. Soc.*, 2021, **143**, 599–603.
55 Y. Ie, Y. Okamoto, S. Tone and Y. Aso, *Chem.–Eur. J.*, 2015, **21**, 16688–16695.
56 T. Ohto, T. Inoue, H. Stewart, Y. Numai, Y. Aso, Y. Ie, R. Yamada and H. Tada, *J. Phys. Chem. Lett.*, 2019, **10**, 5292–5296.
57 H. Bürckstümmer, N. M. Kronenberg, M. Gsänger, M. Stolte, K. Meerholz and F. Würthner, *J. Mater. Chem.*, 2010, **20**, 240–243.
58 H. Bai, Y. Wang, P. Cheng, J. Wang, Y. Wu, J. Hou and X. Zhan, *J. Mater. Chem. A*, 2015, **3**, 1910–1914.
59 Suman and S. P. Singh, *J. Mater. Chem. A*, 2019, **7**, 22701–22729.
60 Y. Che and D. F. Perepichka, *Angew. Chem., Int. Ed.*, 2021, **60**, 1364–1373.
61 A. J. Bard and L. R. Faulkner, *Electrochemical Methods-Fundamentals and Applications*, Wiley, New York, 1984.
62 J. Pommerehne, H. Vestweber, W. Guss, R. F. Mahrt, H. Bässler, M. Porsch and J. Daub, *Adv. Mater.*, 1995, **7**, 551.
63 H. Yamagata and F. C. Spano, *J. Chem. Phys.*, 2012, **136**, 184901.
64 S. T. Turner, P. Pingel, R. Steyrleuthner, E. J. W. Crossland, S. Ludwigs and D. Neher, *Adv. Funct. Mater.*, 2011, **21**, 4640–4652.
65 D. Qian, L. Ye, M. Zhang, Y. Liang, L. Li, Y. Huang, X. Guo, S. Zhang, Z. Tan and J. Hou, *Macromolecules*, 2012, **45**, 9611–9617.
66 W. Zhao, S. Li, H. Yao, S. Zhang, Y. Zhang, B. Yang and J. Hou, *J. Am. Chem. Soc.*, 2017, **139**, 7148–7151.
67 C. Xu, K. Jin, Z. Xiao, Z. Zhao, X. Ma, X. Wang, J. Li, W. Xu, S. Zhang, L. Ding and F. Zhang, *Adv. Funct. Mater.*, 2021, **31**, 2107934.
68 W. Xu, X. Ma, J. H. Son, S. Y. Jeong, L. Niu, C. Xu, S. Zhang, Z. Zhou, J. Gao, H. Y. Woo, J. Zhang, J. Wang and F. Zhang, *Small*, 2022, **18**, 2104215.
69 G. G. Malliaras, J. R. Salem, P. J. Brock and C. Scott, *Phys. Rev. B: Condens. Matter Mater. Phys.*, 1998, **58**, 13411.
70 C. Goh, R. J. Kline, M. D. McGehee, E. N. Kadnikova and J. M. J. Fréchet, *Appl. Phys. Lett.*, 2005, **86**, 122110.
71 S. D. Dimitrov and J. R. Durrant, *Chem. Mater.*, 2014, **26**, 616.
72 C. M. Proctor, J. A. Love and T.-Q. Nguyen, *Adv. Mater.*, 2014, **26**, 5957–5961.
73 J. A. Bartelt, D. Lam, T. M. Burke, S. M. Sweetnam and M. D. McGehee, *Adv. Energy Mater.*, 2015, **5**, 1500577.
74 S. Li, L. Ye, W. Zhao, X. Liu, J. Zhu, H. Ade and J. Hou, *Adv. Mater.*, 2017, **29**, 1704051.
75 K. Chong, X. Xu, H. Meng, J. Xue, L. Yu, W. Ma and Q. Peng, *Adv. Mater.*, 2022, **34**, 2109516.
76 T. Mani, D. C. Grills, M. D. Newton and J. R. Miller, *J. Am. Chem. Soc.*, 2015, **137**, 10979–10991.
77 Y. Song, X. Liu, Y. Li, H. H. Nguyen, R. Duan, K. J. Kubarych, S. R. Forrest and J. P. Ogilvie, *J. Phys. Chem. Lett.*, 2021, **12**, 3410–3416.
78 X. Tan, T. L. Gustafson, C. Lefumeux, G. Burdzinski, G. Buntinx and O. Poizat, *J. Phys. Chem. A*, 2002, **106**, 3593–3598.
79 K. P. Ghiggino, A. J. Tilley, B. Robotham and J. M. White, *Faraday Discuss.*, 2015, **177**, 111–119.
80 A. Saeki, *Polym. J.*, 2020, **52**, 1307–1321.
81 Y. Kobori, T. Ako, S. Oyama, T. Tachikawa and K. Marumoto, *J. Phys. Chem. C*, 2019, **123**, 13472–13481.
82 P. J. Hore, D. A. Hunter, C. D. McKie and A. J. Hoff, *Chem. Phys. Lett.*, 1987, **137**, 495–500.
83 G. L. Closs, M. D. E. Forbes and J. R. Norris, *J. Phys. Chem.*, 1987, **91**, 3592–3599.
84 M. Hasegawa, H. Nagashima, R. Minobe, T. Tachikawa, H. Mino and Y. Kobori, *J. Phys. Chem. Lett.*, 2017, **8**, 1179–1184.
85 M. Van Landeghem, W. Maes, E. Goovaerts and S. Van Doorslaer, *J. Magn. Reson.*, 2018, **288**, 1–10.
86 O. Gonen and H. Levanon, *J. Phys. Chem.*, 1984, **88**, 4223–4228.
87 T. Biskup, M. Sommer, S. Rein, D. L. Meyer, M. Kohlstadt, U. Wurfel and S. Weber, *Angew. Chem., Int. Ed.*, 2015, **54**, 7707–7710.
88 L.-M. Wang, Q. Li, S. Liu, Z. Cao, Y.-P. Cai, X. Jiao, H. Lai, W. Xie, X. Zhan and T. Zhu, *ACS Appl. Mater. Interfaces*, 2020, **12**, 24165–24173.
89 R. J. Collins and D. A. Kleinman, *J. Phys. Chem. Solids*, 1959, **11**, 190–194.
90 Y. Firdaus, V. M. L. Corre, S. Karuthedath, W. Liu, A. Markina, W. Huang, S. Chattopadhyay, M. M. Nahid, M. I. Nugraha, Y. Lin, A. Seitkhan, A. Basu, W. Zhang, I. McCulloch, H. Ade, J. Labram, F. Laquai, D. Andrienko, L. J. A. Koster and T. D. Anthopoulos, *Nat. Commun.*, 2020, **11**, 5220.
91 S. Jinnai, Y. Ie, M. Karakawa, T. Aernouts, Y. Nakajima, S. Mori and Y. Aso, *Chem. Mater.*, 2016, **28**, 1705–1713.
92 S. Jinnai, Y. Ie, Y. Kashimoto, H. Yoshida, M. Karakawa and Y. Aso, *J. Mater. Chem. A*, 2017, **5**, 3932–3938.
93 M. J. Frisch, *et al.*, *Gaussian 16 A. 01*, Gaussian, Inc., Wallingford CT, 2009.
94 Y. Kobori and T. Miura, *J. Phys. Chem. Lett.*, 2015, **6**, 113–123.
95 T. Miura, M. Aikawa and Y. Kobori, *J. Phys. Chem. Lett.*, 2014, **5**, 30–35.
96 Y. Kobori, R. Noji and S. Tsuganezawa, *J. Phys. Chem. C*, 2013, **117**, 1589–1599.